Delft University of Technology

Experimental Investigation of Vortex Flow Over a Flying V Subsonic Transport

van Luijk, N.L.M.; Vos, Roelof

Citation (APA)
van Luijk, N. L. M., & Vos, R. (2025). Experimental Investigation of Vortex Flow Over a Flying V Subsonic Transport. In *Proceedings of the AIAA SCITECH 2025 Forum* Article AIAA 2025-0258 (AIAA Science and Technology Forum and Exposition, AIAA SciTech Forum 2025). https://doi.org/10.2514/6.2025-0258

Important note
To cite this publication, please use the final published version (if applicable).
Please check the document version above.

Experimental Investigation of Vortex Flow over a Flying V Subsonic Transport

Nikki van Luijk* and Roelof Vos†

Delft University of Technology, 2629HS Delft, The Netherlands

Blunt-nosed, highly-swept crescent wings, often found in flying wing designs like the Flying V, offer high aerodynamic efficiency but exhibit nonlinear aerodynamic behavior at high angles of attack. This study experimentally investigates the vortical flow over the Flying V under these conditions at a Reynolds number of 8.0×10^5 and a Mach number of 0.10. Balance measurements assess the aerodynamic performance, while oil flow visualization captures the on-surface flow topology. A 7-hole pressure probe maps the off-surface flow topology above the wing's suction side. Results reveal a double vortex system (in- and outboard vortex) forming over the inboard wing starting at $\alpha = 12.5°$. At $\alpha = 15.0°$, the stronger outboard vortex merges with another vortex over the outboard wing, which develops aft of the leading-edge kink at $\alpha = 7.5°$. The vortical flow enhances the aerodynamic performance through vortex lift between $\alpha = 10.0°$ and 18.0°. However, at the latter angle, a pitch break occurs, attributed to the breakdown of the inboard vortex and the upstream movement of its onset and breakdown locations. Balance data indicate that the vortex breakdown is asymmetric, occurring first over the starboard wing.

Nomenclature

b	Semi-wing span [m]		**Greek Symbols**	
$\overline{c}$	Mean aerodynamic chord [m]		α	Angle of attack [°]
C_D	Drag coefficient [-]		λ_2	Lambda2-criterion [1/s²]
C_l	Rolling moment coefficient [-]		λ_{Ci}	LambdaCi-criterion [1/s]
C_L	Lift coefficient [-]		ω_x	Axial vorticity [1/s]
C_m	Pitching moment coefficient [-]			
L	Aircraft length [m]		**Superscripts**	
M	Mach number [-]		˜	Normalized
Q	Q-criterion [1/s²]			
Re_c	Reynolds number based on $\overline{c}$ [-]		**Acronyms**	
S	Reference area [m²]		A	Attachment Line
u	Axial velocity [m/s]		MAC	Mean Aerodynamic Chord
U_∞	Free-stream velocity [m/s]		S	Separation Line
x, y, z	Cartesian coordinates [m]		SL	Shear Layer

I. Introduction

The rise in extreme weather events in 2023 highlights the accelerating pace of climate change, with record heat waves, droughts, wildfires, and floods affecting millions worldwide [*]. To combat this, industries, including aviation, must

---

*PhD Candidate, Faculty of Aerospace Engineering

†Associate Professor, Faculty of Aerospace Engineering, Associate Fellow AIAA

*2023 – a year of climate extremes, Max-Planck-Gesellschaft. Retrieved on 22-05-2024 from `https://www.mpg.de/21506133/2023-a-year-of-climate-extremes`

adopt sustainable practices. The aviation sector is working towards this by promoting Sustainable Aviation Fuel (SAF) and biofuels, which could reduce CO_2 emissions by 65% by 2050 [†]. However, SAF and biofuels are not a complete solution, as they still emit CO_2 and cost 1.5 to 6 times more than traditional kerosene [‡], potentially limiting air travel to the wealthy. Along the same lines, further advancements in aircraft and engine technology itself can only take us so far regarding emission reductions. Specifically, the improvements in aircraft energy efficiency in the past decade have been much smaller compared to those seen 50 years ago, suggesting that a technological plateau has been reached [1]. Since alternative fuels and technology alone cannot fully address the sustainability problem, a long-term solution must be found elsewhere.

Such a long-term solution is to rethink aircraft conceptual design by merging the payload bay with the lifting surfaces, reducing the wetted area per unit of useful volume. This creates configurations called Blended-Wing-Bodies (BWBs) and Flying Wings (FWs), which can increase the lift-to-drag ratio by at least 10-15% compared to tube-wing aircraft [2]. An example is the Flying V, where the payload bay is integrated into the V-shaped wing [3], as shown in Figure 1. It offers a 20% lift-to-drag ratio improvement over aircraft like the Airbus A350 [4]. The payload bay placement results in an inboard wing with a blunt nose and a thick airfoil, producing adverse transonic effects. However, these effects are mitigated by a high-inboard-wing sweep angle, which delays the onset of strong shock waves. In contrast, the outboard wing features a lower sweep angle, which benefits control surface effectiveness. This configuration gives the Flying V a planform best described as a blunt-nosed, highly-swept crescent wing - a wing with a lower quarter-chord sweep angle in the outboard wing compared to the inboard wing and a trailing edge that is non-straight.
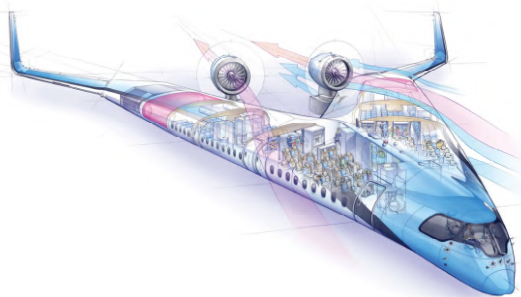

Fig. 1   Schematic view of the Flying V [§].

Whereas the transonic performance of crescent-winged BWBs and FWs can be optimized by reducing the wetted area and adjusting the wing sweep, studies have shown complex vortical flow structures and nonlinear aerodynamic effects at high angles of attack for these configurations. For the Flying V, Viet's open-jet wind tunnel experiments confirmed this by revealing the existence of at least three vortices: two over the inboard wing and one at the leading-edge kink, accompanied by a strong pitch break at an angle of attack of 20° [5]. The existence of the kink vortex aligns with earlier findings on (sharp-nosed) double-delta wings by Verhaagen et al. [6–8], where the apex and kink vortices could merge, thereby stabilizing the flow and delaying vortex breakdown depending on the inflow angle and wing geometry. Similar vortex behavior was observed on another typical crescent-winged BWB, where the blended wing-fuselage junction produced complex vortex behavior, as reported by Arora et al. [9]. Despite experimental and numerical efforts, these complex vortical flows remain poorly understood.

Besides the leading-edge kink, the leading-edge bluntness was found to play an important role in the development of the vortical flow. This motivated NATO'S International Vortex Experiment 2 (VFE-2), aimed at understanding the governing flow phenomena related to highly-swept, blunt-nosed wings in high-angle-of-attack conditions [10]. Using a 65° delta wing with interchangeable leading edges in both wind tunnel campaigns and simulations, the study revealed that blunt-nosed wings generate two distinct leading-edge vortices, with the outboard being the stronger one. Additionally, they form aft of the leading edge rather than at the leading edge, which is the case for sharp-nosed wings [11–13]. Subsequent NATO studies on the Stability and Control Configuration (SACCON) investigated a varying leading-edge bluntness along the wing span, revealing that the flying wing produced three leading-edge vortices at or behind the different leading-edge radii sections [14–16]. However, the detailed flow physics remained unknown.

[†]Net zero 2050: Sustainable Aviation Fuels. Retrieved on 25-01-2024 from https://www.iata.org/en/iata-repository/

[‡]Current Landscape and Future of SAF Industry. Retrieved on 18-11-2024 from https://www.easa.europa.eu/eco/eaer/topics/sustainable-aviation-fuels/current-landscape-future-saf-industry

[§]Greener Skies Ahead: Take a look inside the Flying V. Retrieved on 19-11-2024 from https://www.nationalgeographic.com/

Despite prior efforts, a complete picture of the vortical flow structures over blunt-nosed crescent-winged aircraft like the Flying V is still missing from the open literature. It is also unclear how these flow structures compare to those over blunt-nosed delta wings or how the leading-edge kink influences the blunt-nosed vortex flow. The current study aims to experimentally identify the governing flow structures over such wings under high-angle-of-attack conditions using the Flying V. This paper presents the experimental setup in Section II and the results of the wind tunnel experiment in Section III. Hypothesis and observations are summarized in Section IV.

II. Experimental Setup

This section outlines the experimental setup for the wind tunnel campaign conducted in the Low Turbulence Tunnel at Delft University of Technology. The overview begins with a description of the wind tunnel facility in Section II.A, which provides the framework for the experimental setup. The wind tunnel model is subsequently detailed in Section II.B. Finally, Sections II.C and II.D present the measurement techniques and test conditions used.

A. Wind Tunnel Facility

The wind tunnel campaign is conducted in the Low Turbulence Tunnel (LTT), a closed-return low-speed tunnel with a maximum velocity of 120 m/s. The experiments presented in this study are performed at a free-stream velocity of 35 m/s, corresponding to a mean aerodynamic chord-based Reynolds number of $Re_c = 8.0 \times 10^5$ at $\bar{c} = 0.34$ m, and a Mach number of $M = 0.10$. Further details on the test conditions are provided in Section II.D.

The LTT features a removable octagonal test section of 1.8 m wide and 1.25 m tall, with diverging walls that eliminate the need for buoyancy corrections in balance data. These diverging walls compensate for the streamwise pressure gradient caused by the boundary layer development on the wind tunnel walls, yielding a zero-pressure gradient in an empty wind tunnel. Figure 2 shows the model setup in the octagonal test section. The moment reference point used for force and moment measurements, explained in Section II.C, is visualized in Figure 2a.
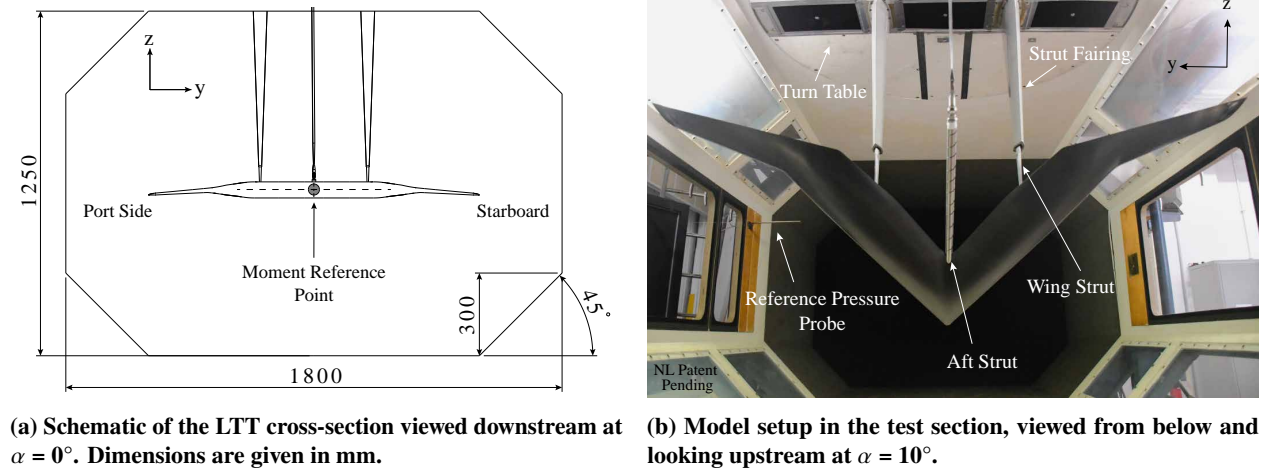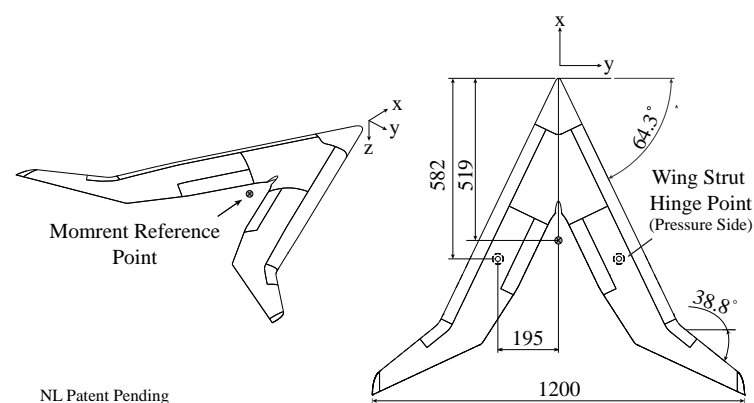

(a) Schematic of the LTT cross-section viewed downstream at $\alpha = 0°$. Dimensions are given in mm.

(b) Model setup in the test section, viewed from below and looking upstream at $\alpha = 10°$.

Fig. 2   Overview of the model setup in the LTT of the TU Delft with an inverted model suspension.

The name *Low Turbulence Tunnel* is derived from its turbulence limit of 0.02% for a free-stream velocity below 40 m/s. Its maximum turbulence level of 0.07% is attained at a free-stream velocity of 75 m/s [17]. The tunnel also features a three-point support system that suspends the model upside down, connecting it to the external balance located above the test section. The three-point support system comprises two wing struts and an aft strut, as visualized in Figure 2b. A wire is wrapped around the aft strut to control the vortex shedding from this cylindrical support. Furthermore, fairings, which are not connected to the external balance, shield the wing struts from the flow. In addition to supporting the model weight and forces, the wing struts function as hinge points, allowing the model to be pitched to adjust the angle of attack. The test section is completed by the turntable in the ceiling, which ensures that the model and the balance can be rotated to adjust the yaw angle, and the glass panel located in the floor to provide optical access.

3

B. Wind Tunnel Model

As discussed in Section I, the Flying V represents a prime example of a blunt-nosed, crescent-winged aircraft. The transonically optimized Flying V design by Laar [18, 19] is therefore used as the geometry for the purpose-built wind tunnel model. A full-span model with a total span of 1.2 m is developed, corresponding to a 1.84% scale model. The span is limited to minimize the blockage effects at high angles of attack while maintaining the model's structural integrity. Geometric details of the model are shown in Figure 3 and Table 1, including the reference system and moment reference point used for the measurements explained in Section II.C.

The model is designed to be modular, allowing various geometries to be tested in future experiments. This includes options to evaluate different leading-edge designs, trailing-edge engine configurations, cockpit or nosecone shapes, and winglet or wing tip designs. The modular components are shown in Figures 3 and 5, where the dark lines represent production breaks in the model. For this study, the Flying V's winglets are replaced by simple Küchemann wing tips to eliminate the effect of the winglets on the vortical flow development over the wing. Lastly, the model is suspended upside down in the wind tunnel using wing and aft struts as discussed in Section II.A. The wing strut locations on the pressure side are highlighted in Figure 3, which serve as hinge points for adjusting the model's pitch attitude.

Parameter	Value	Unit
Span (b)	1200	mm
Reference area (S)	0.307	m^2
Reference point (x_{ref})	519	mm
MAC ($\overline{c}$)	338	mm
Scale	1.84	%

Table 1   Wind tunnel model specifications, based on the Flying V design by Laar [18, 19].

Fig. 3   Technical drawing of the modular wind tunnel model, based on the Flying V design by Laar [18, 19]. Dimensions are in mm.

C. Measurement Techniques

The vortical flow over the Flying V is investigated using the LTT's external balance, a digital 7-hole pressure probe, and the oil flow technique. These methods capture the on- and off-surface flow topology as well as the overall aircraft performance in terms of force and moment coefficients. Each measurement technique is discussed in more detail below.

1. External Balance

The external balance above the test section is a 6-component mechanical system that allows for adjustments in the angle of attack and yaw angle. Unlike internal balances based on strain gauges, it is nearly insensitive to temperature variations and creep. Additionally, it offers high accuracy across a large range of forces. Based on the expected forces and moments, the balance measurements have an uncertainty of ±0.02 N [20, 21], corresponding to ±8.7x10^{-5} for the force coefficients in this study. Measurements are recorded at 500 Hz for 5 seconds per data point and are averaged to mitigate vibrations and disturbances. Repetitions of the measurements are spread over two to three days, ensuring repeatability. The moment reference point for the data is the leading edge of the mean aerodynamic chord mapped onto the symmetry plane of the model, which is visualized in Figures 2a and 3.

Due to the design of the test section as discussed in Section II.A, no buoyancy corrections are required for the resulting forces and moments. However, other corrections, such as those for interference and blockage effects, are not applied either. This is because the classical analytical methods are not suited to unconventional configurations like the Flying V. Previous attempts to numerically estimate these corrections using RANS simulations of the current experimental setup show poor correlation with the experimental results, highlighting the complexity of the flow under investigation [22]. Consequently, no reliable wind tunnel corrections are currently available for the Flying V.

4

2. Flow Visualization

The oil flow visualization technique is used to capture the on-surface flow topology by applying a mixture of paraffin oil and UV-luminescent particles to the model. The mixture follows the shear stress vectors acting on the model's surface under the influence of the flow, and the resulting patterns can be visualized using UV light. Images are captured using a DSLR camera positioned beneath the glass floor panel of the test section. A UV filter is used on the camera lens to reduce reflections from the UV light on the glass panel. It is important to note that increasing the angle of attack causes the nose of the model to tilt downward, which could introduce gravitational effects on the transportation of the oil, specifically in low-shear flow areas. However, the viscosity of the oil mixture is tested iteratively to develop a mixture that minimizes the gravitational effects, even in low-shear areas.

3. 7-Hole Pressure Probe

A digital 7-hole pressure probe is used to capture off-surface flow fields. The 7-hole probe used in this campaign contains an internal pressure scanner, eliminating the need for pressure tubes connected to an external scanner, thereby avoiding possible data lags due to the tube length. The probe is moved by mounting it on a sting, which is connected to a traversing system downstream of the test section, see Figure 4.
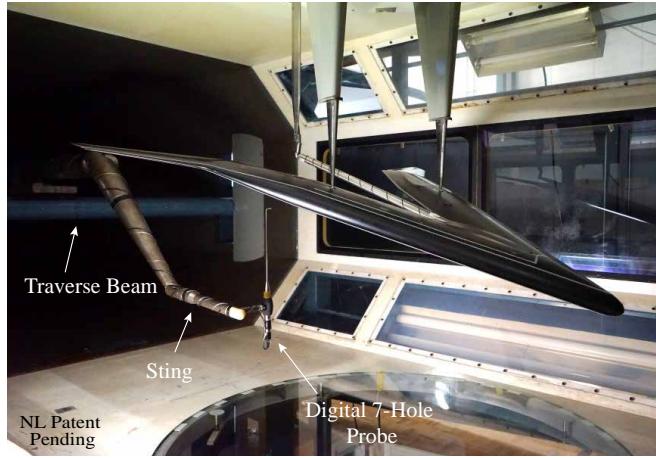

Fig. 4 Setup of the digital 7-hole probe system on the traverse beam and sting in the LTT.
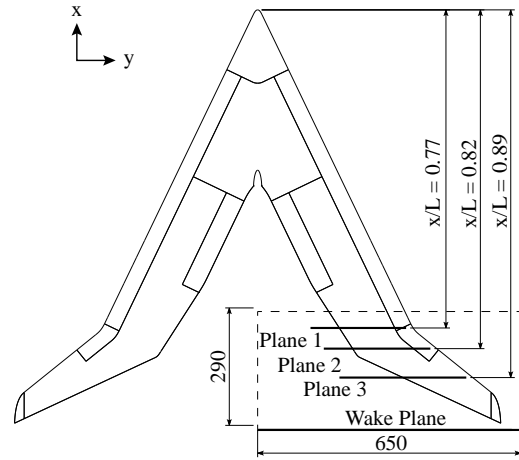

Fig. 5 Schematic of the 7-hole probe measurement planes and traverse's reach (dashed line).

Although the setup tries to minimize the probe and sting area inserted into the flow region of interest, it is important to note that the presence of the probe could still induce premature vortex breakdown [23]. Payne et al. observed that inserting a probe into the flow over a delta wing shifts the vortex breakdown location upstream of the probe when the natural breakdown occurs at the trailing edge, where it is inherently less stable due to the strong adverse pressure gradient [24]. Furthermore, the vortex breakdown location is more sensitive to probe interference on low-sweep delta wings than on highly-swept ones [24]. Also the probe size plays an important role, as Sforza et al. found: a 9.8 mm probe head induced early vortex breakdown on an 80° delta wing, whereas a 3.2 mm probe did not [25]. The 7-hole probe used in this study has a 2.0 mm head, and the high wing sweep, particularly in the inboard region, minimizes the expected interference. However, pressure probe measurements fundamentally cannot determine the exact natural breakdown location due to unavoidable interference effects.

Measurements are taken on three vertical planes positioned perpendicular to the free-stream flow above the suction surface. Data is recorded with a horizontal resolution of 3.0 mm (x-direction) and at 500 Hz in the vertical direction (z-direction). The locations of the measurement planes are determined based on prior Flying V wind tunnel tests [5] and the physical constraints of the wind tunnel setup, such as the traverse system's reach, as shown in Figure 5. Planes 1 and 2 are placed upstream and downstream of the leading-edge kink to assess its effect, while Plane 3 captures the vortices over the outboard wing. The planes remain perpendicular to the free-stream flow as the angle of attack increases. Additionally, the planes are positioned 10 mm above the suction surface to avoid channel flow effects and the strong pressure and velocity gradients in the boundary layer, which cause erroneous readings. Additional measurements are taken 10 mm behind the wing tip in the wake at selected angles of attack to investigate the flow further.

5

During post-processing, the pressure data from the 7-hole probe is converted into velocity components, flow angles, and total and static pressures using the calibration algorithm developed by Shaw-Ward et al. [26]. Subsequently, several vortex detection criteria are applied to the obtained 3D flow components using Tecplot 360 [¶]. These criteria, outlined in Table 2, each have specific advantages and limitations. A combination of these methods allows vortex structures to be identified more accurately. Note that the criteria are normalized based on the mean aerodynamic chord and the free-stream velocity as indicated by the tilde.

Table 2   Overview of vortex detection criteria, including their descriptions, strengths, and limitations [27, 28].

Criterion	Normalized Variable	Description	Vortex Condition	Strengths & Limitations
Axial vorticity [27]	$\tilde{\omega}_x$	Strength of the local rotational motion	$\|\tilde{\omega}_x\| > ...$	+ Indicates rotational direction - Needs a threshold
Q-criterion [27]	$\tilde{Q}$	Ratio between vorticity and shear in a flow	$\tilde{Q} > 0$	+ Simple, low computational cost - $\tilde{Q} < 0$ in high shear flows with vortices
Lambda2-criterion [27]	$\tilde{\lambda}_2$	Local pressure min. without unsteady straining or viscosity, based on the 2nd largest eigenvalue of the strain rate & vorticity tensor combined	$\tilde{\lambda}_2 < 0$	+ Allows to compare relative strength using $\|\tilde{\lambda}_2\|$ - Sensitive to noise
LambdaCi-criterion [28]	$\tilde{\lambda}_{Ci}$	Vortex swirling strength based on the imaginary eigenvalues of the velocity gradient tensor	$\tilde{\lambda}_{Ci} > 0$	+ More robust, less dependent on grid resolution - Only identifies coherent vortical flow structures, no filaments

D. Test Conditions

The campaign is conducted at a free-stream velocity of 35 m/s, corresponding to a mean aerodynamic chord-based Reynolds number of 8.0×10^5 and a Mach number of 0.10. Although the LTT can reach speeds up to 120 m/s, the test velocity is limited to avoid model vibrations and deformations observed at higher speeds. It is hypothesized that these vibrations result from 3D flow phenomena occurring at high angles of attack. Higher flow velocities also increase free-stream turbulence levels and support interference. Therefore, the chosen test velocity is a trade-off between scaling requirements and wind tunnel effects.

To minimize scaling effects, zig-zag tape is applied to ensure boundary layer similarity between the wind tunnel's low Reynolds number and the full-scale Reynolds number of 63.0×10^6. The tape, which is 6 mm wide with a roughness of 0.255 mm and 70° angles, induces subgrid-scale vortices, promoting boundary layer transition. The tape is positioned at 5% x/c on the suction side and 10% x/c on the pressure side, with the local chord measured perpendicular to the leading edge. As the angle of attack increases, the stagnation point shifts aft on the pressure side, requiring the tape to move aft. However, at high angles of attack, this shift becomes so pronounced that a second tape is applied at 20% x/c on the pressure side ahead of the wing struts to ensure flow transition across the entire angle of attack range.

The angle of attack ranges from 0.0° to 27.0°, with the upper limit defined by the physical limitations of the external balance and support system. Balance measurements are taken in 1.0° increments, while oil flow visualizations are obtained between 0.0° and 25.0° in 2.5° increments. The 7-hole probe measurements are performed between 0.0° and 20.0° in 2.5° increments, capturing regions of interest identified in previous research by Viet [5]. Finally, wake measurements are conducted at angles of attack of $\alpha = 0.0°$, 10.0°, and 15.0° to investigate the flow state further.

[¶]Tecplot 360. Retrieved on 27-11-2024 from https://tecplot.com/products/tecplot-360/

III. Results & Discussion

This section presents the results of the study on vortex flow over the Flying V, a blunt-nosed, highly-swept crescent wing. Data is collected at a free-stream velocity of 35 m/s, corresponding to Re_c = 8.0x10^5 and M = 0.10. Measurements are taken over an angle of attack range between 0.0° to 27.0°, as discussed in Section II.D.

The prior study by Viet [5] forms the foundation for the current investigation into the vortex aerodynamics of the Flying V, as discussed in Section I. Using balance measurements, along with oil flow, smoke, and tuft visualizations, the flow topology was investigated on a half-model of the Flying V in an open-jet wind tunnel [5]. Multiple leading-edge vortices were observed forming over the inboard wing starting at α = 13.0°, while a single vortex developed over the outboard wing at α = 11.0°. Balance measurements revealed a strong pitch break at α = 20.0° with the moment reference point at 25%$\bar{c}$ [5]. However, the data was insufficient to identify its cause. Despite geometric and experimental differences between Viet's study and the current investigation, the overall trends are expected to be similar.
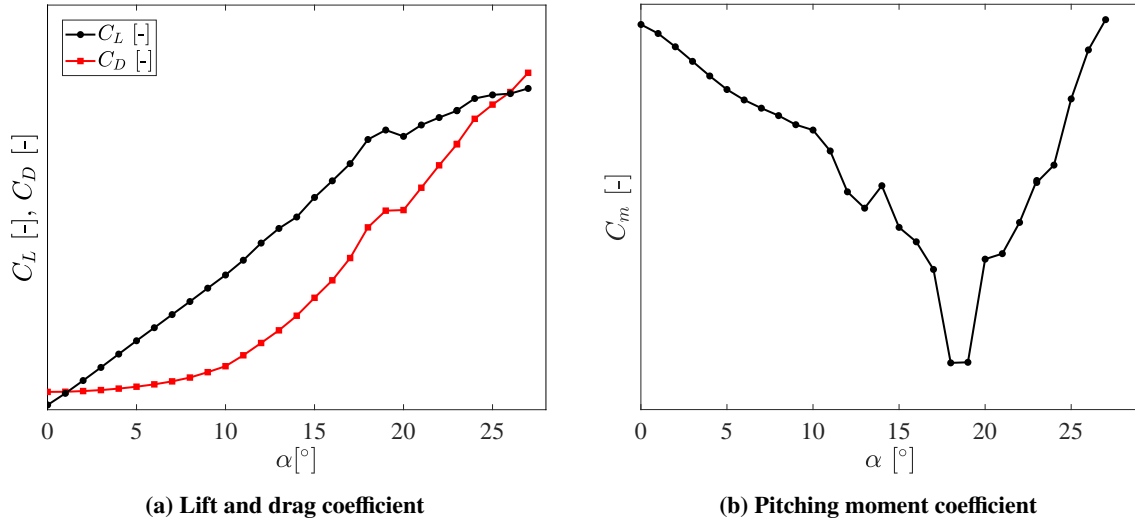

(a) Lift and drag coefficient

(b) Pitching moment coefficient

Fig. 6 Symmetric force and moment coefficients at Re_c = 8.0x10^5 and M = 0.10.

The obtained symmetric force and moment coefficients confirm this; see Figure 6. A strong pitch break occurs at α = 19.0°, with a shallow positive C_{m_α} slope starting at α = 18.0°. Using the same reference point location as Viet [5] but scaled to the current model yields a more pronounced slope increase at α = 18.0°, indicating the start of the pitch break. Despite the -2.0° difference in the pitch break angle, the overall C_L and C_m behavior is similar. The trends in the force and moment coefficients are further analyzed by linking their behavior to the underlying flow physics derived from the on- and off-surface flow data. Since the 7-hole probe data begins 10 mm above the surface, streamlines derived from the velocity data are extrapolated onto the surface by matching them with flow features in the oil flow patterns, which are indicated on the following figures by *S*, *A* and *SL* for separation and attachment lines, and shear layers, respectively.

Furthermore, as discussed in Section II.C, various vortex criteria are applied to identify vortical flow, as illustrated in Figure 12 (p. 14). For clarity, only the normalized axial vorticity is presented for the other data points to illustrate the rotational direction, although all criteria are considered when identifying the vortex structures. Note that the reference system used in these vorticity plots coincides with the moment reference point shown in Figures 2a and 3. The analysis of the flow physics is structured based on the four flow regimes identified: 1) attached flow (Section III.A), 2) vortical flow onset (Section III.B), 3) vortical flow development (Section III.C), and 4) vortical flow with breakdown (Section III.D). Finally, the identified flow physics are synthesized to provide a complete overview of the aircraft performance and limitations of the data in Section III.E.

Note that specific details of the Flying V geometry cannot be disclosed. Instead, airfoils with similar characteristics are used in the vorticity plots to indicate the relative position of the wing and the data, as shown in Figure 12 (p. 14). Specifically, the airfoils visualized in the contour plots are the *NACA63(4)-421*, *NACA63-412*, and *NASA SC(2)-0706* for measurement Planes 1, 2, and 3, respectively. It is important to note that the measurement planes are perpendicular to the free-stream direction. As a result, the flow in these plots is directed out of the plane, and the data represents the cross flow across the measurement planes.

A. Attached Flow

The attached flow regime for the Flying V is limited to low angles of attack up to 5.0°. Under these conditions, little to no flow separation is observed, as shown in the oil flow image in Figure 7. Nonetheless, cross flow is present near the trailing edge of the inboard wing, moving in the outboard direction. The cross-flow region exhibits low shear forces, as indicated by the meandering lines in the oil flow pattern. The low shear forces suggest that the cross-flow region will be one of the first to separate as the angle of attack increases.

The low-shear area also blocks the predominantly streamwise flow from the wing's leading edge, resulting in a distinct line where oil accumulates between the two flow directions, as highlighted in Figure 7. While oil accumulation often indicates a separation line, in this case, the flow remains attached with mass transfer occurring in the downstream direction. In other words, the accumulation line represents a shear layer between the intersecting flow regions. A similar shear layer was also observed in Viet's earlier experiments [5]. However, due to the upright orientation of the half-model, gravitational effects strongly influenced the low-shear areas. Combined with the use of a thin oil mixture, this led to the oil flow being pulled downward as the shear forces declined, thereby reducing the similarity between the two studies.
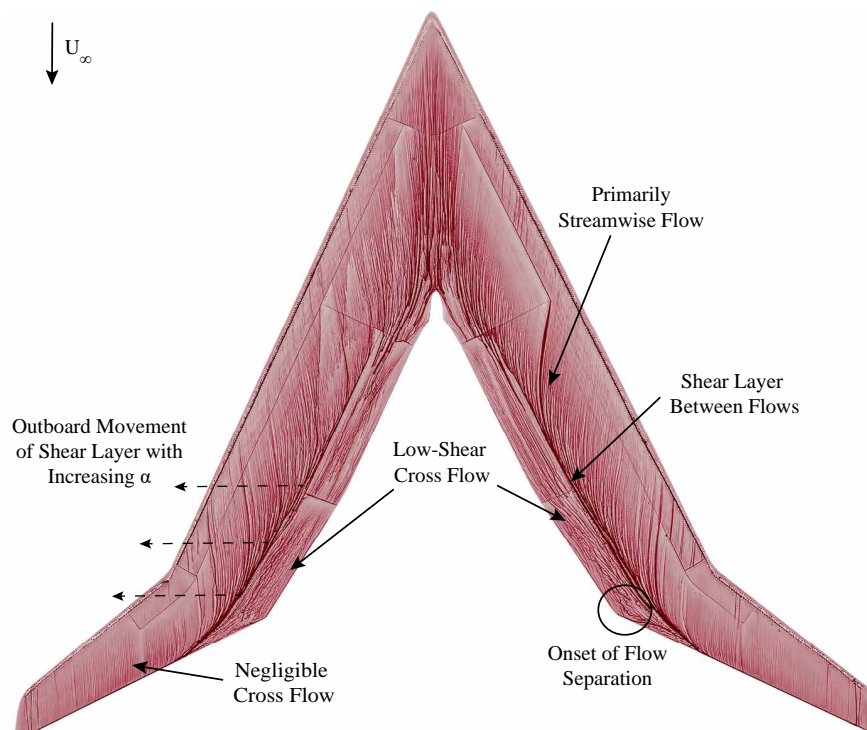

Fig. 7   Oil flow and annotated flow features at $\alpha = 0.0°$, with $Re_c = 8.0 \times 10^5$ and $M = 0.10$.

Wake measurements using the 7-hole probe at $\alpha = 0.0°$ confirm that the flow is mostly attached along the wingspan and contains weak cross-flow components. The small wake has a minimum axial velocity of u/U_∞ equal to 0.60, with an average of 0.75, and features a weak wing tip vortex. Nevertheless, a small region on the wing near the trailing-edge kink shows early signs of flow separation, as shown in Figure 7. In contrast, the outboard wing exhibits a fully attached flow with a negligible cross-flow component. However, as the angle of attack increases, the flow begins to change. The shear layer between the two flow regions is pulled closer to the leading edge and shifts outboard due to the increased strength of the leading-edge suction at higher angles of attack, see Figure 7. Consequently, the low-shear region, which remains on the verge of being attached, grows in size. Additionally, the initial signs of flow separation at the trailing-edge kink develop into a region of actual flow separation.

As the angle of attack increases further, balance measurements suggest a worsening of the flow separation. That is, the drag coefficient rises by 29% between $\alpha = 0.0°$ and 5.0°, and by an additional 51% as the angle increases to $\alpha = 8.0°$. This rise in drag coefficient suggests the growth of the area of flow separation.

8

B. Vortical Flow Onset

As indicated by the increased drag at higher angles of attack, flow separation becomes more pronounced from $\alpha = 5.0°$ onward. This is evident in the oil flow image presented in Figure 8, which also shows the measurement plane locations and derived off-surface (cross-)flow topology at these planes at $\alpha = 7.5°$. Compared to Figure 7, the shear layer between the low-shear cross flow and the streamwise leading-edge flow shifts further outboard. Flow across the planes converges toward this shear layer, which acts as a flow sink where mass transportation occurs in the downstream direction. As this flow sink moves outboard, the flow curvature above the wing becomes stronger to converge into the sink, resulting in a higher vorticity in this flow region. The flow curvature is visible in the flow topology at measurement Planes 1 and 2 drawn in Figure 8. Simultaneously, the trailing-edge separation area continues to grow in the upstream direction along the inboard-wing trailing edge.

In addition to the growing regions of flow separation and curvature, a vortical flow structure is observed at the trailing edge of the inboard wing. This clockwise trailing-edge vortex, labeled as vortex V1 in Figure 8, transports flow from the pressure side to the suction side around the highly-swept trailing edge. Mirande et al. [29] identified a similar trailing-edge vortex in water tunnel experiments on a 60° aft-swept thick wing and noted significant interactions with the main vortex above the wing. In contrast, Poll [30] did not observe such vortices on swept wings with leading-edge sweep angles of 56° or less, possibly due to the differences in measurement techniques, as Poll's study did not involve off-surface flow visualizations. Alternatively, the trailing-edge vortex may be a characteristic of wings with a leading edge-sweep angle greater than 56°.
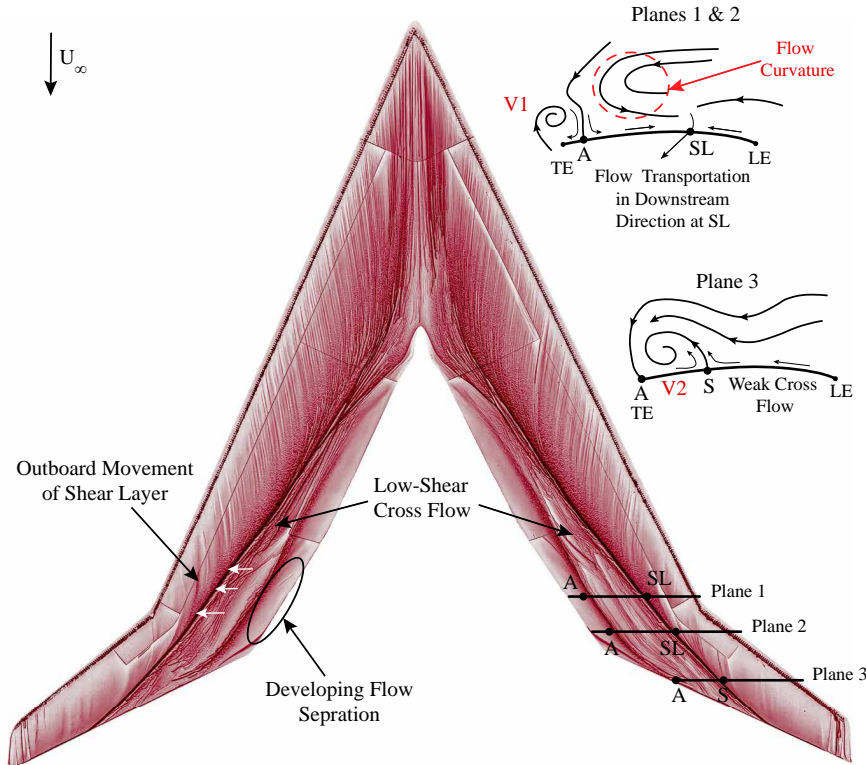

Fig. 8   Oil flow and cross-flow topology, viewed upstream at $\alpha = 7.5°$, with $Re_c = 8.0\text{x}10^5$ and $M = 0.10$.

Downstream of the leading-edge kink, the so-called kink vortex V2 is identified above the outboard wing at measurement Plane 3. The vortex is believed to be weak, leaving no clear trace in the oil flow pattern at this stage. The origin of the vortex is the shear layer developing on the inboard wing, which likely transitions into a separation line under the influence of geometric changes in the leading-edge kink area. V1 and V2 may begin forming prior to $\alpha = 7.5°$; however, the 10 mm data gap between the measurement planes and wing surface prevents confirmation. Since the oil flow patterns on the inboard wing at $\alpha = 7.5°$ and 5.0° are similar, it is believed that trailing-edge vortex V1 begins developing at the lower angle of attack. This is supported by the significant strength of V1 at $\alpha = 7.5°$, with a value of $\tilde{\lambda}_{Ci} = 13.0$ and $\tilde{\omega}_x = -30.4$ in its core.

As the angle of attack increases to 10.0°, the flow becomes increasingly complex. The drag coefficient continues to rise, as shown in Figure 6a, due to additional trailing-edge flow separation. Simultaneously, the lift curve slope increases from $\alpha = 10.0°$ onward, indicating the onset of vortex lift contribution. The angle of attack of 10.0° also corresponds to the onset of asymmetric oil flow patterns on both wing halves, likely caused by asymmetric vortex formation. These asymmetries could originate from small asymmetries in the flow, model geometry, or surface quality, particularly in the leading-edge kink region where the inboard wing transitions into the outboard wing. Such sensitivity to small asymmetries was previously noted for vortex breakdown by Pfnür et al. [31]. The asymmetries in the oil flow are evident in Figure 9, such as the weaker flow separation on the port side outboard wing, where the separation line does not extend toward the trailing edge. Note that a UV light reflection is visible near the wing root, which should not be interpreted as a flow feature.
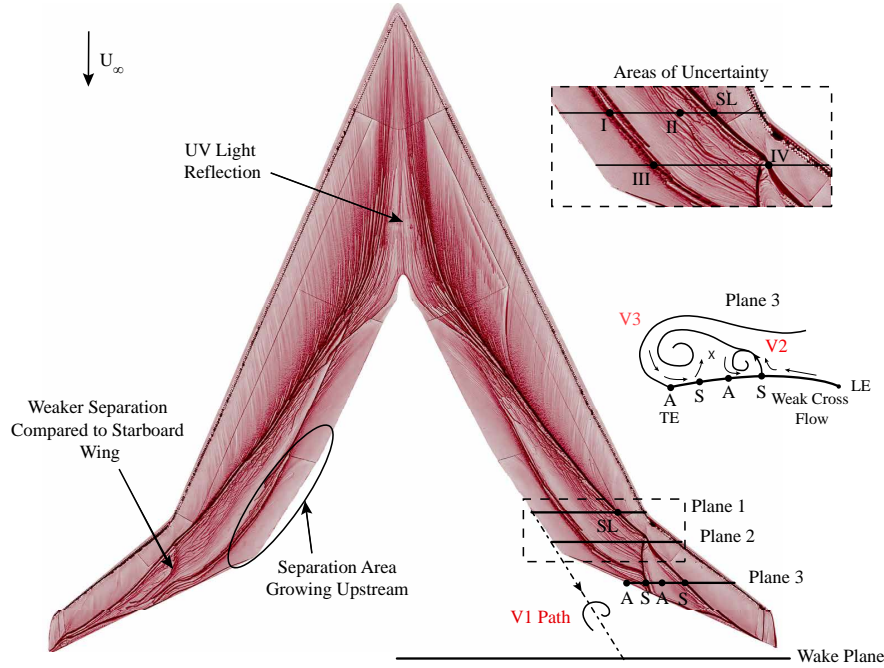

Fig. 9   Oil flow and cross-flow topology, viewed upstream at $\alpha = 10.0°$, with $Re_c = 8.0 \times 10^5$ and $M = 0.10$.

Next to the asymmetries, some features in the oil flow remain ambiguous, making it impossible to draw conclusions about the off-surface flow topology in the 10 mm data gap above the wing surface. Consequently, the streamlines on Planes 1 and 2 cannot be extrapolated to the oil flow for $\alpha = 10.0°$. These areas of uncertainty, marked with Roman numerals in Figure 9, represent flow features that could not be confidently identified as separation or attachment lines or other distinct flow features. The 7-hole probe data above the inboard wing does show that the counter-clockwise flow curvature above the trailing edge intensifies as the axial vorticity at specific points almost doubles to $\tilde{\omega}_x = 24.6$ compared to $\alpha = 7.5°$ (see Figure 8). Additionally, the size and vorticity magnitude of V1 increase, with the normalized swirl strength $\tilde{\lambda}_{Ci}$ being approximately 2.2 times higher than at $\alpha = 7.5°$ ($\tilde{\lambda}_{Ci} = 28.6$) with a more concentrated axial vorticity yielding a value of $\tilde{\omega}_x = -61.2$.

On the other hand, the oil flow near measurement Plane 3, combined with the 7-hole probe data, is less ambiguous, which allows for the derivation of the off-surface flow topology, as shown in Figure 9. This reveals that the region of high vorticity above the inboard wing's trailing edge closes into vortex V3 above the outboard wing, positioned inboard of the existing vortex V2. As V3 forms, its axial velocity decreases while its axial vorticity becomes stronger and more concentrated yielding $\tilde{\omega}_x = 50.8$ in its core, which is accompanied by a swirl strength of $\tilde{\lambda}_{Ci} = 20.3$, though it remains weaker than V1 on the inboard wing. Additionally, V3 is a wake-like vortex with $u/U_\infty < 1.0$ in its core. Such wake-like velocity profiles have been observed in wing tip vortices and at low Reynolds numbers for flows over non-slender delta wings [32–35]. In contrast, slender wings tend to produce jet-like vortices, where $u/U_\infty > 1.0$ [32].

While there is no complete consensus on the onset of vortex breakdown, it is generally associated with the development of a stagnation point on the longitudinal axis of the vortex, which is followed by a zone of reversed flow [36]. This suggests that wake-like vortices may be closer to breakdown than jet-like vortices. However, the axial velocity

measured by the 7-hole probe does not necessarily represent the axial velocity of the vortex, as the probe is aligned with the free-stream flow, while the vortex cores are most likely not. The misalignment is confirmed by the oil flow combined with off-surface flow data at $\alpha = 12.5°$, see Figure 10a, which shows that V2 follows a path parallel to the leading edge of the outboard wing rather than the free-stream direction.

Despite the oil flow being inconclusive for $\alpha = 10.0°$ on the inboard wing, vortex V1 is captured in the wake measurements. Its position suggests it leaves the wing's surface at the trailing-edge kink. The wake measurements also reveal the strong effect of the cross flow over the inboard wing, which pushes all the flow outboard, resulting in the phenomenon of *wake filling*. As a result, a wing wake is only present behind the outboard wing. Nevertheless, the wake remains consistent with mostly attached flow over the outboard wing with a strong wing tip vortex identified by the vortex criteria.
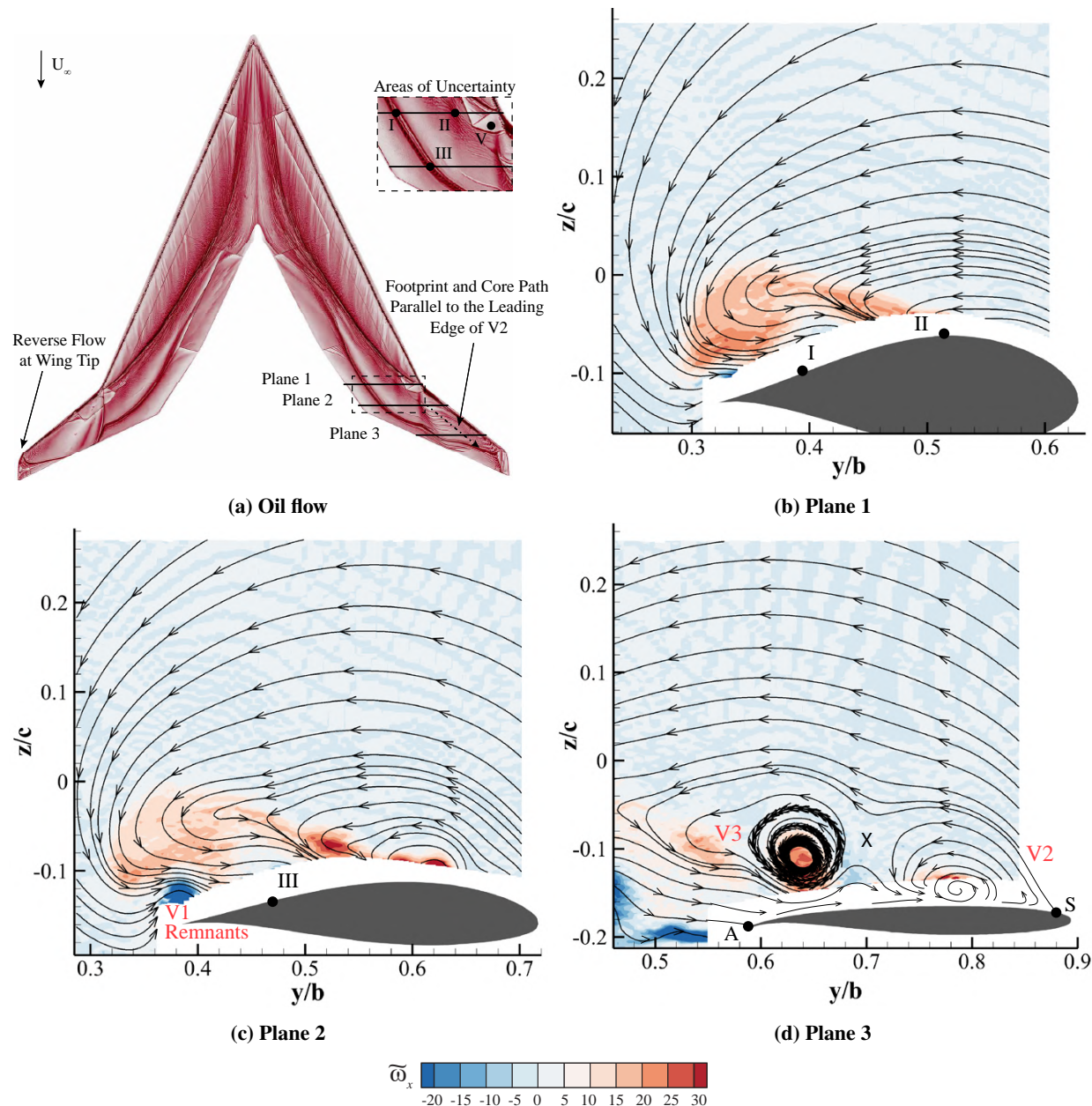

(a) Oil flow

(b) Plane 1

(c) Plane 2

(d) Plane 3

Fig. 10   Oil flow and normalized axial vorticity with cross-flow topology, viewed upstream at $\alpha = 12.5°$, with Re_c = 8.0x10^5 and M = 0.10.

The vortex onset continues to develop as the angle of attack increases to 12.5°. The oil flow on the inboard wing remains relatively similar to that at $\alpha = 10.0°$, see Figures 9 and 10a, including the areas of uncertainty that remain and partially overlap between the cases. However, the outboard wing now clearly shows reverse flow at the wing tip and a vortex footprint, following a path parallel to its leading edge. This vortex, V2, is captured in Planes 2 and 3 in Figure 10, indicating that the core lifts up from the surface. On the other hand, both vortices V2 and V3 are visible in the streamlines at Plane 3 in Figure 10d. The densification of the streamlines at vortex V3 indicates a higher rate of downstream mass transportation in that area.

Although the core of vortex V2 lies within the 10 mm data gap at Plane 3, the values for u/U_∞ at its edges suggest that the vortex is jet-like. In contrast, vortex V3, which remains wake-like, exhibits a 37% decrease in swirling strength ($\tilde{\lambda}_{Ci} = 12.8$) and significant dispersion of its axial vorticity, now measuring almost 50% less ($\tilde{\omega}_x = 26.8$) compared to the flow at $\alpha = 10.0°$. Despite the weakening of V3, the increase in axial velocity of V2 contributes to the rise in vortex lift and the decrease in the pitching moment derivative, as seen in Figure 6. Notably, vortex V1 is no longer present on the inboard wing ahead of the leading-edge kink, with only weak remnants of the vortex visible at Plane 2 (Figure 10c), as the flow no longer meets the vortex conditions listed in Table 2. The disintegration of V1 is attributed to the growing trailing-edge separation, which reduces the pressure difference between the pressure and suction sides of the wing.

C. Vortical Flow Development

As the angle of attack increases, the vortical flow develops further, revealing the formation of another vortex. For $\alpha = 15.0°$, the oil flow and axial vorticity at the measurement planes are shown in Figure 11. Compared to Figure 10 at $\alpha = 12.5°$, the onset of V3 shifts upstream. Additionally, the formation of the new vortex V4 at Plane 1 (in Figure 11b) creates a double-vortex system with V3 on the inboard wing. This system resembles the flow structures observed over blunt-nosed delta wings during the VFE-2 experiments discussed in Section I [10, 12, 37, 38]. The onset mechanisms of the double-vortex system could be similar [37]: where the inboard vortex originates from boundary layer effects due to a 3D bubble-type laminar-turbulence transition, forming a weaker vortex. However, no clear evidence is observed in the oil flow to support this similarity. In contrast, the outboard vortex may result from the local reduction in leading-edge bluntness caused by the blending of the inboard wing towards the outboard wing, where the leading edge is inherently sharper. The sharper nose, combined with the cross flow from the trailing edge moving to the inboard wing's leading edge, potentially produces the outboard vortex V4.

Consistent with the findings of the VFE-2 [10, 12, 37, 38], the outboard vortex V4 is stronger than the inboard V3. At Plane 2, V4 reaches a swirling strength of $\tilde{\lambda}_{Ci} = 28.0$ with a concentrated region of vorticity with a maximum of $\tilde{\omega}_x = 61.6$ in its core, and a jet-like velocity profile ($u/U_\infty = 1.4$). On the other hand, V3 has a swirling strength of $\tilde{\lambda}_{Ci} = 12.5$ with a more dispersed vorticity pattern with a maximum of $\tilde{\omega}_x = 21.3$, and a slightly lower axial velocity ratio of 1.2. Besides confirming the VFE-2 findings, this data also shows that the upstream motion of V3's onset yields a jet-like vortex rather than a wake-like vortex seen at $\alpha = 12.5°$ and a more dispersed axial vorticity. Additionally, at Plane 2, the remnants of V1, see Figure 11c, disappeared. The disintegration of V1 is attributed to the reduced pressure difference between the pressure and suction surfaces, as well as the formation of the larger counter-rotating vortices over the wing, which can interact with the trailing-edge vortex, as observed by Mirande et al. [29].

It must be noted that only two vortices are clearly captured at Plane 2; V3 and V4 (Figure 11c). However, outboard of vortex V4, the axial vorticity suggests another counter-clockwise vortex below the measurement plane. This is likely kink vortex V2, which is merging with the stronger co-rotating vortex V4. The merged vortex, still labeled V4, is weaker after merging, with a swirling strength of $\tilde{\lambda}_{Ci} = 8.1$ and an axial velocity ratio of $u/U_\infty = 0.6$, showing a 71% and 57% decrease, between Planes 2 and 3. Additionally, the concentrated axial vorticity disperses with a maximum value of $\tilde{\omega}_x = 22.5$ in its core, as shown in Figure 11d. The dispersion and weakening indicate that V4 is becoming unstable after merging with V2. Moreover, at Plane 3, a secondary vortex could potentially form underneath the separation bubble shown in Figure 11d, while the vorticity layer originating from the pressure side at the trailing edge of Plane 3 may develop into a vortex downstream in the wake.

Finally, wake measurements at $\alpha = 15.0°$ reveal significant differences compared to lower angles of attack. The outboard wing exhibits a large wake with a minimum $u/U_\infty = 0.20$ between $y/b = 0.75$ and 1.0 and no wing tip vortex, indicating that the outboard wing flow separates. The flow separation is asymmetric, as indicated by the oil flow patterns in Figure 11a. On the port side, the separation line is drawn toward and sticks to the trailing edge of the outboard wing, indicating stronger flow separation compared to the starboard side, where the separation line does not reach the trailing edge. The separation is also reflected in the pitching moment coefficient shown in Figure 6b. While C_m decreases

12

rapidly between α = 10.0° and 13.0° due to the developing vortex lift of V2, a local instance with C_{m_α} > 0 is observed at an angle of attack of 14.0°. This slope increase coincides with a local decrease in the lift curve slope at α = 14.0°. These variations in C_m and C_L are linked to the outboard wing flow separation at α = 14.0°, which temporarily reduces lift downstream of the moment reference point. However, the increasing vortex lift from V3 and V4 with increasing angle of attack compensates for the reduced lift due to the flow separation, restoring the negative value for the pitching moment derivative until vortex breakdown appears over the outboard wing.
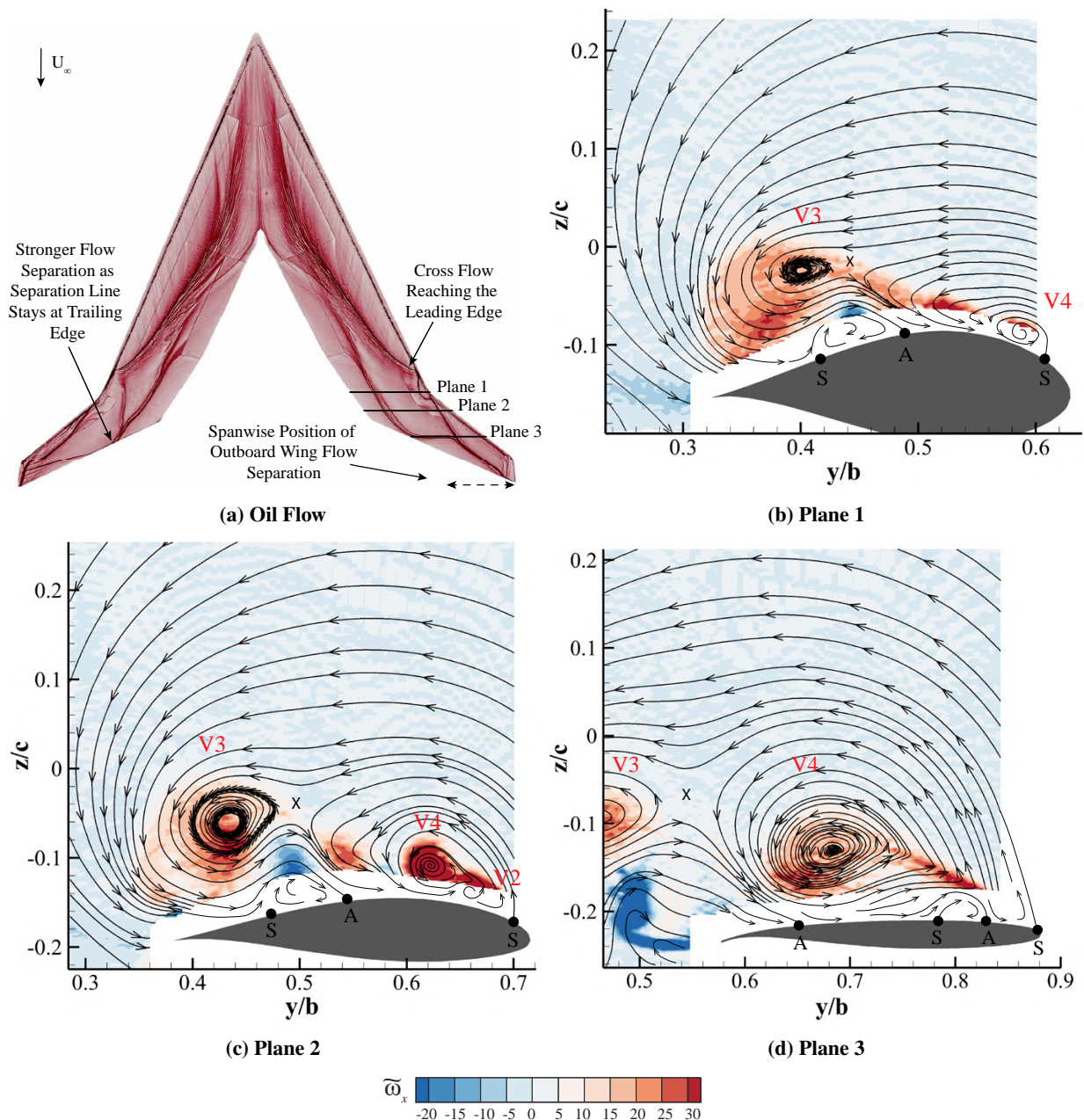

(a) Oil Flow

(b) Plane 1

(c) Plane 2

(d) Plane 3

Fig. 11   Oil flow and normalized axial vorticity with cross-flow topology, viewed upstream at α = 15.0°, with Re_c = 8.0x10^5 and M = 0.10.

13

D. Vortical Flow with Breakdown

Vortex breakdown is first observed at an angle of attack of 17.5° over the outboard wing. The inboard wing flow is, nonetheless, similar to that at α = 15.0°, as shown in Figures 11 and 13. The main difference is that the vortex cores are lifted up from the surface, consistent with an increase in the angle of attack. Additionally, both V3 and V4 over the inboard wing exhibit jet-like velocity profiles in their cores, with V3's swirl strength increasing by 54% compared to α = 15.0°, indicative of a maturing vortex. Figure 12 illustrates all vortex criteria at Plane 1 to provide a better understanding of the flow. Similar to the results discussed in Section III.C, V4 remains significantly stronger than V3. Furthermore, V3 is expected to break down before V4 according to the findings of the VFE2-studies [10, 12, 37, 38].
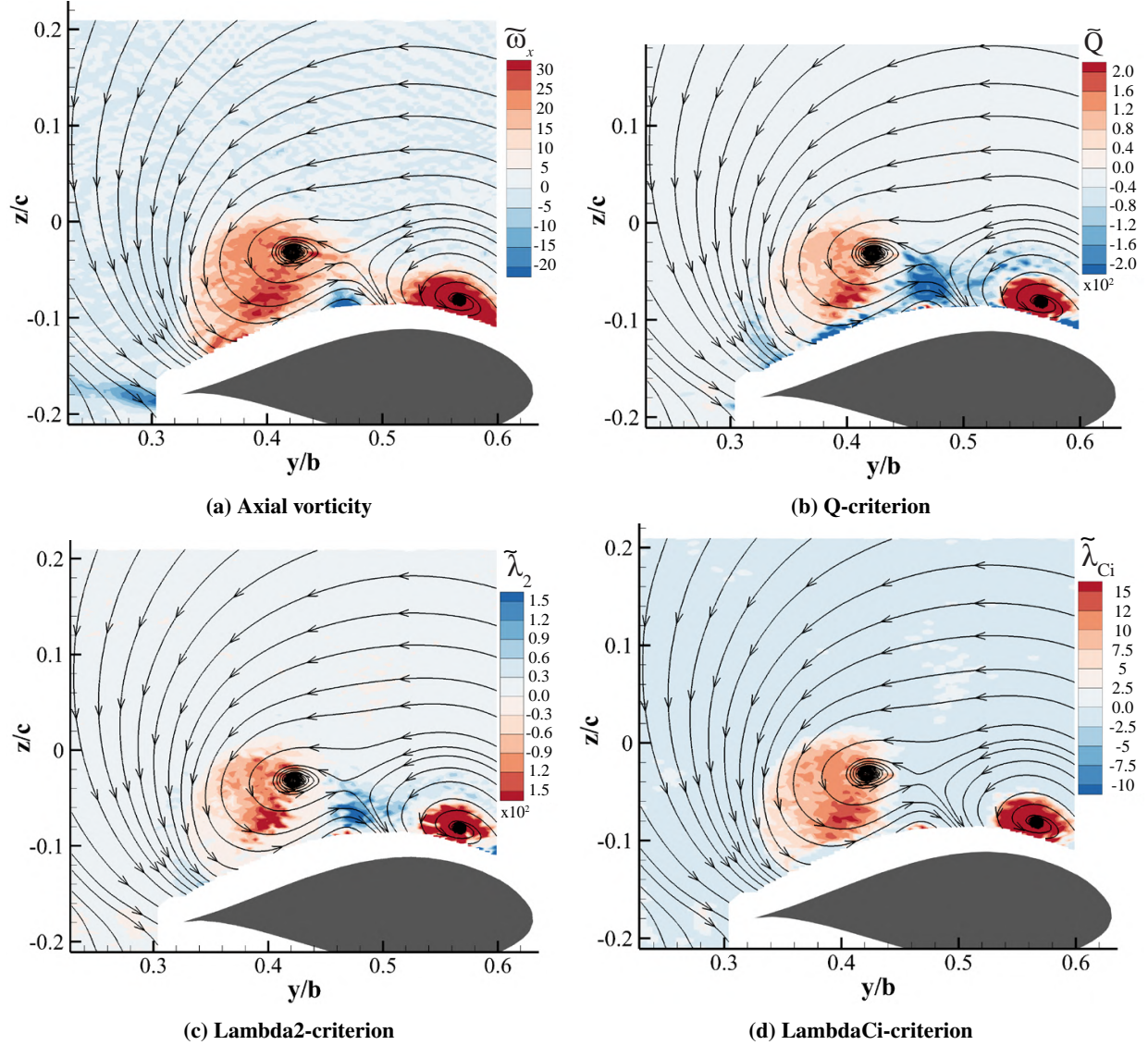

(a) Axial vorticity

(b) Q-criterion

(c) Lambda2-criterion

(d) LambdaCi-criterion

Fig. 12   Normalized vortex criteria with cross-flow topology at Plane 1, viewed upstream at α = 17.5°, with Re_c = 8.0x10^5 and M = 0.10.

The anticipated breakdown of vortex V3 is confirmed when looking at the outboard wing Plane 3 in Figure 13d, where vortex V3 begins breaking down and starts merging with vortex V4. This unsteady process results in the incoherent streamlines recorded by the 7-hole probe. The merging strengthens V4, particularly its axial vorticity, which increases by 42% to $\tilde{\omega}_x$ = 31.9 compared to the conditions at α = 15.0°. Nonetheless, its vorticity remains dispersed, similar to Figure 11d. It is hypothesized that the increase in vorticity is partly due to the separated outboard wing flow, which feeds additional vorticity into vortex V4. The strengthening of V4 results in more vortex lift, yielding a more

negative C_{m_α} and a more positive C_{L_α}, which is observed in Figure 6 at α = 17.5°. The lift coefficient locally peaks right after, at an angle of attack of 19.0°.

Note that V4 showed signs of becoming unsteady at α = 15.0°, while V3 enters breakdown first. It is theorized that V4 undergoes a more gradual breakdown, whereas V3 experiences an abrupt breakdown. Viviani et al. [39] also observed gradual vortex breakdown over a blended-wing-body, attributing it to the local boundary layer properties and surface curvature, in contrast to the abrupt breakdown typically associated with vortices. Additionally, studies on double delta wings suggest that the leading-edge kink distance influences the nature of the vortex breakdown as well by affecting the vortex interaction [40, 41]. Besides geometrical effects, inboard vortices on blunt-nosed delta wings decay downstream due to viscous effects in combination with less separated flow being sucked into its core due to the formation of the stronger outboard vortex [42]. For the Flying V, it is likely that a combination of these factors results in the breakdown of the inboard vortex V3 prior to the outboard vortex V4.

(a) Oil Flow

(b) Plane 1

(c) Plane 2

(d) Plane 3

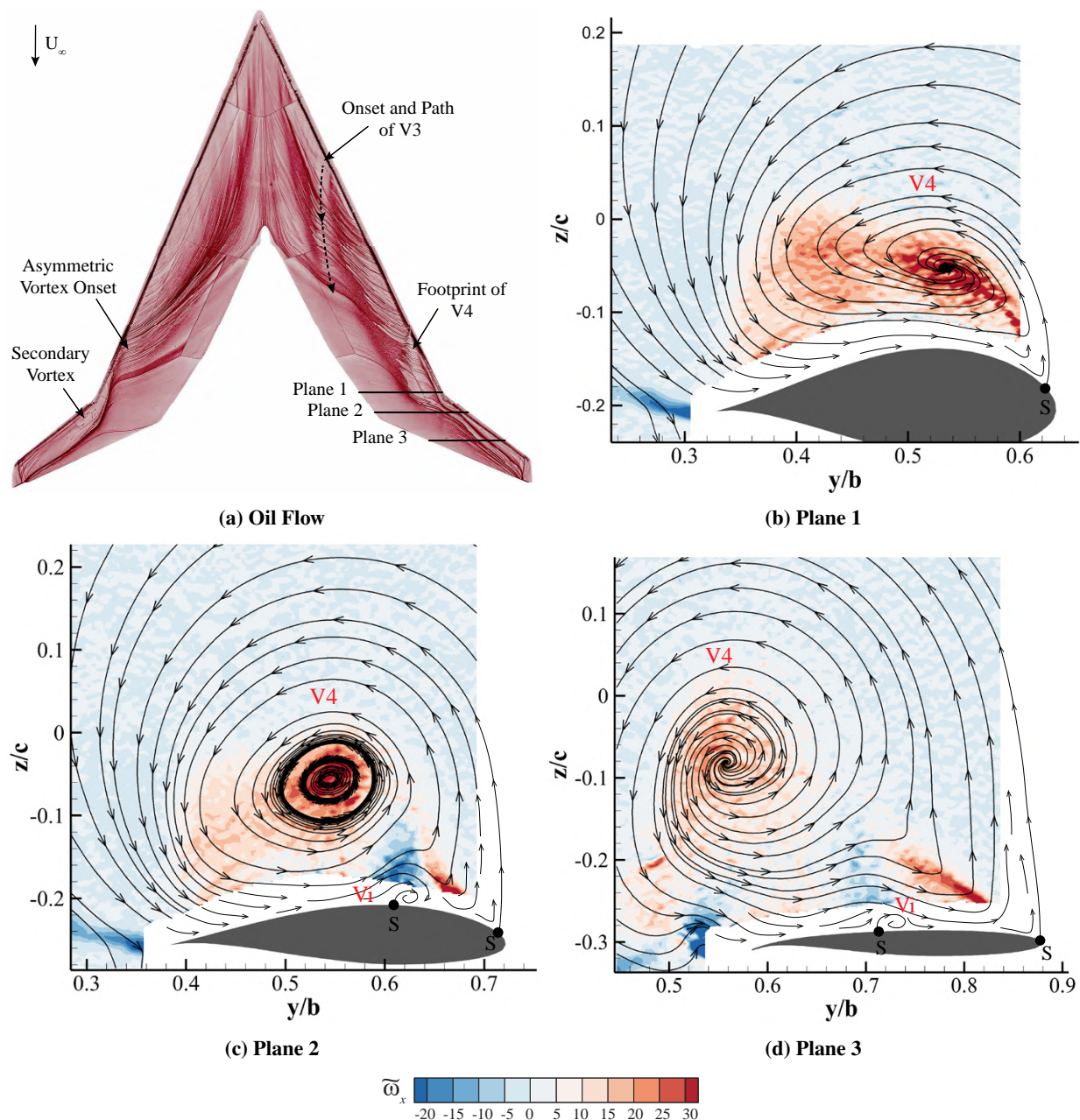**Fig. 13   Oil flow and normalized axial vorticity with cross-flow topology, viewed upstream at α = 17.5°, with Re_c = 8.0x10⁵ and M = 0.10.**

15

After the pitch break, at an angle of attack of 20.0°, the on- and off-surface flow topology is visualized in Figure 14. These figures represent the flow state right after the pitch break at $\alpha = 18.0°$ (Figure 6b). V3 is no longer captured on any of the 7-hole probe measurement planes, though its onset and footprint remain visible in the oil flow shown in Figure 14a. The oil flow pattern shows that the onset of V3 has moved upstream and inboard beyond the field of view of the measurement planes. Given that V3's breakdown occurred near Plane 3 at $\alpha = 17.5°$, and knowing that the breakdown location of a vortex moves upstream with increasing angle of attack [37], V3's breakdown is likely above the inboard wing at $\alpha = 20.0°$.

(a) Oil Flow

(b) Plane 1

(c) Plane 2

(d) Plane 3

Fig. 14 **Oil flow and normalized axial vorticity with cross-flow topology, viewed upstream at $\alpha = 20.0°$, with Re_c = 8.0x10^5 and $M = 0.10$.**

In contrast, V4 remains visible on the measurement planes. Its size increases, with the core shifting up from the surface and inboard, consistent with an upstream movement of the onset location at higher angles of attack. Additionally, a secondary vortex Vi can be derived at Planes 2 and 3 (Figure 14c and 14d), though weak, thereby leaving no traces in

the oil flow patterns. At the angle of attack of 20.0°, V4 reaches its peak strength at Plane 2, with a swirling strength of $\tilde{\lambda}_{Ci}$ = 17.3 with a relatively concentrated axial vorticity of $\tilde{\omega}_x$ = 37.9 and a jet-like velocity profile with u/U_∞ = 1.4. After reaching its peak strength, V4 becomes weaker at Plane 3 with an axial velocity ratio nearing unity and with reductions in the swirling strength of 44% ($\tilde{\lambda}_{Ci}$ = 9.7), and 46% in the axial vorticity ($\tilde{\omega}_x$ = 20.4). The axial vorticity also becomes more dispersed, suggesting that V4 may be entering breakdown as it can no longer feed off the leftovers of V3. At higher angles of attack, this trend is anticipated to continue, with the core of V4 moving up and inboard while weakening and going into breakdown. Additionally, the onset of V3 moves upstream, which is evident from the footprint in the oil flow, and Vi becomes more pronounced, leaving traces in the oil flow patterns at α = 22.5° and 25.0°.

E. Flow Physics Synthesis

The presented data allows for an overall understanding of the flow development over the Flying V and highlights points of attention regarding the scalability of the results. A significant finding is the sequence of events leading to the observed pitch break. This sequence likely begins with the breakdown of the inboard vortex V3 starting at α = 17.5°, which subsequently progresses upstream as the angle of attack increases. Once the vortex breakdown and onset locations move past the critical limit, more lift is generated ahead of the moment reference point, causing the sudden change in the sign of the pitching moment derivative at α = 18.0°. The flow state change is reflected in the lift curve, where the lift coefficient drops immediately after the pitch break, as shown in Figure 6a. The stabilization of the drag coefficient between α = 19.0° and 20.0° may result from the complete disintegration of V3 over the outboard wing, thereby reducing the pressure drag.

Figure 15 shows an overview of the flow physics at critical points in the pitching and rolling moment coefficient behavior to provide a complete picture of the events leading to the pitch break. Notably, slope changes in both coefficients coincide, starting at α = 10.0° where vortex lift starts to play a role. Subsequently, at α = 14.0°, the outboard wing flow separates, generating a rolling moment toward the starboard wing, indicating that the separation likely starts on this wing half. In contrast, the increasing strength of outboard vortex V4 from α = 15.0° onward induces a rolling moment toward the port side, combined with a nose-down pitching moment just before the pitch break. At α = 18.0°, the pitch break occurs, accompanied by a pitch-up moment resulting from the loss of vortex lift on the outboard wing. Simultaneously, a strong rolling moment is induced toward the starboard wing, suggesting that the pitch break is likely caused by vortex breakdown over this wing half. Vortex breakdown on the port side is hypothesized to occur around α = 20.0°, indicated by the change in sign of the rolling moment coefficient derivative, followed by an increase in the pitching moment derivative from α = 21.0° onward. The asymmetric breakdown sequence aligns with the observed asymmetric oil flow patterns from α = 10.0° onward.
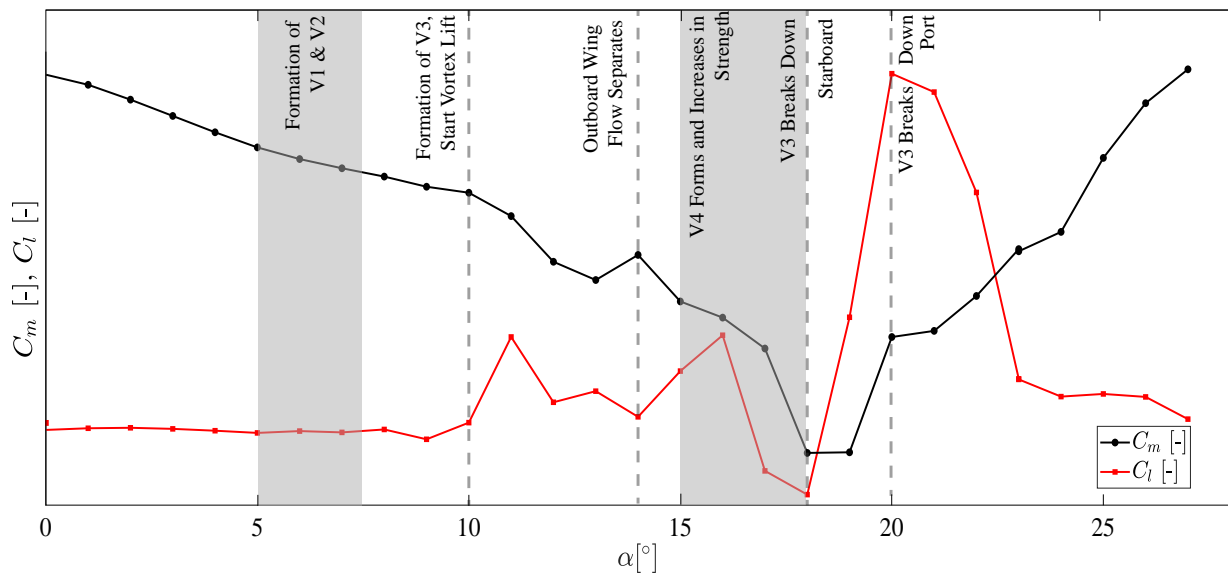

Fig. 15 Pitching and rolling moment coefficients with flow development annotations at Re_c = 8.0x10⁵ and M = 0.10.

17

Note that the slope of the pitch break starting at $\alpha = 18.0°$ depends on the location of the moment reference point. When the reference point is at the leading edge of the mean aerodynamic chord as used in this study, the strong pitch break begins at an angle of attack of 19.0°, while a small positive C_{m_α} slope starts at $\alpha = 18.0°$. Shifting the reference point upstream results in a negative slope at $\alpha = 18.0°$, but the strong pitch break remains at an angle of 19.0°. Inversely, moving the reference point downstream increases the positive C_{m_α} slope at $\alpha = 18.0°$, clearly indicating the start of the pitch break at this angle. Nevertheless, the strong pitch break caused by the disintegration and upstream movement of the inboard vortex V3 remains between $\alpha = 18.0°$ and 19.0° for all cases.

However, caution is warranted as the measurement technique used to capture the vortex breakdown could induce the breakdown itself. As discussed in Section II.C, inserting a probe into the flow may artificially move the breakdown location ahead of the probe. This could influence the sequence of events leading up to the pitch break described in Figure 15. Given the small size of the probe head, the probe interference is expected to be minimal. Nonetheless, there is a -2.0° difference in the pitch break angle between the current study and Viet's work [5], using the same moment reference point. The earlier onset of vortex breakdown is likely due to both probe interference and the change in geometry of the Flying V between the studies. Since the geometrical changes to the Flying V were significant, the probe interference is expected to be small.

Another limitation of the study is the low Reynolds number at which the experiments are conducted. Despite the application of zig-zag tape to simulate transition (see Section II.D), the thick boundary layer has different properties compared to the full-scale conditions. Similar to blunt-nosed delta wings at decreasing Reynolds numbers, the onset locations are expected to shift, with the outboard vortex forming further upstream and the inboard vortex forming further inboard compared to the full-scale case. Additionally, the outboard vortex becomes relatively stronger than the inboard vortex at lower Reynolds numbers [37], potentially affecting the onset of the pitch break.

IV. Conclusion & Recommendations

This study provides new insights into the complex vortex flow over the Flying V, a blunt-nosed, highly-swept crescent wing commonly found on sustainable aircraft. Wind tunnel experiments on a model of the Flying V reveal the flow topology and aerodynamic characteristics at high angles of attack, using oil flow visualization, balance measurements, and 7-hole pressure probe data. The main findings include the formation of a double-vortex system (in- and outboard vortex) above the inboard wing starting at $\alpha = 12.5°$. This is consistent with the double-vortex system observed over blunt-nosed delta wings, where the outboard vortex is significantly stronger. A vortex forming aft of the leading-edge kink over the outboard wing at $\alpha = 7.5°$ co-rotates and merges with the outboard vortex from $\alpha = 15.0°$ onward. Additionally, a trailing-edge vortex driven by the pressure difference around the trailing edge exists up to 15.0°, after which it dissipates due to the increased flow separation at the trailing edge, reducing the pressure difference. At a higher angle of attack of $\alpha = 18.0°$, the pitching moment derivative becomes positive. This sign change coincides with the inboard vortex's breakdown above the outboard wing and the upstream shift of its onset and breakdown locations. Rolling moment data shows that the pitch break starts with vortex breakdown over the starboard wing, highlighting the asymmetric nature of these flows.

While the overall flow behavior is clear from this study, the detailed mechanisms behind the vortex onset and breakdown remain unclear, highlighting the need for further research. Future studies should employ non-invasive techniques and explore higher Reynolds numbers to assess the scalability of these findings to full-scale aircraft. Nonetheless, this work advances the understanding of vortex flows over unconventional crescent-wing configurations, contributing to the knowledge relevant to sustainable aircraft design.

References

[1] Zheng, X. S., and Rutherford, D., "Fuel Burn of New Commerical Jet Aircraft: 1960 to 2019," Tech. rep., The International Council on Clean Transportation (ICCT), September 2020.

[2] Okonkwo, P., and Smith, H., "Review of evolving trends in blended wing body aircraft design," *Progress in Aerospace Sciences*, Vol. 82, 2016, pp. 1–23. https://doi.org/10.1016/j.paerosci.2015.12.002.

[3] Benad, J., "The Flying V - A new Aircraft Configuration for Commercial Passenger Transport," *Proceedings of the Deutscher Luft- und Raumfahrtkongress (DLRK)*, 2015, pp. 1–8. https://doi.org/10.25967/370094.

[4] Oosterom, W., "Flying V Family Design," Master's thesis, Delft University of Technology, Delft, The Netherlands, 2021.

[5] Viet, R., "Analysis of the Flight Characteristics of a Highly Swept Cranked Flying Wing By Means of an Experimental Test," Master's thesis, Delft University of Technology, Delft, The Netherlands, 2019.

[6] Verhaagen, N., "An Experimental Investigation of the Vortex Flow over Delta and Double-Delta Wings at Low Speed," Tech. rep., University of Technology Delft, 1983.

[7] Hoeijmakers, H., Vaatstra, W., and Verhaagen, N., "On the Vortex Flow over Delta and Double-Delta Wings," *3rd Joint Thermophysics, Fluids, Plasma and Heat Transfer Conference*, American Institute of Aeronautics and Astronautics (AIAA), St. Louis, MO, U.S.A, 1982. https://doi.org/10.2514/6.1982-949.

[8] Verhaagen, N., "Investigation of the Vortex Flow Over a 76/60-deg Double Delta Wing at 20 deg Incidence," *9th Applied Aerodynamics Conference*, American Institute of Aeronautics and Astronautics (AIAA), Baltimore, MD, USA, 1991. https://doi.org/10.2514/6.1991-3208.

[9] Arora, A., Das, S., and Kumar, P., "Flow Field Investigation of a Blended Wing Body in Low Speeds," *Journal of Applied Fluid Mechanics*, Vol. 16, No. 4, 2023, pp. 794–804. https://doi.org/10.47176/jafm.16.04.1475.

[10] AVT-113, NATO RTO, "Understanding and Modeling Vortical Flows to Improve the Technology Readiness Level for Military Aircraft," Tech. Rep. RTO-TR-AVT-113, NATO Research & Technology Organisation, October 2009. https://doi.org/10.14339/RTO-TR-AVT-113.

[11] Luckring, J., "Transonic Reynolds Number and Bluntness Effects for a 65-deg Delta Wing," *41st Aerospace Sciences Meeting and Exhibit*, American Institute of Aeronautics and Astronautics (AIAA), Reno, Nevada, USA, 2003. https://doi.org/10.2514/6.2003-753.

[12] Luckring, J. M., "Initial experiments and analysis of blunt-edge vortex flows for VFE-2 configurations at NASA Langley, USA," *Aerospace Science and Technology*, Vol. 24, No. 1, 2013, pp. 10–21. https://doi.org/10.1016/j.ast.2012.02.005.

[13] Mitchell, A. M., and Délery, J., "Research into vortex breakdown control," *Progress in Aerospace Sciences*, Vol. 37, No. 4, 2001, pp. 385–418. https://doi.org/10.1016/S0376-0421(01)00010-0.

[14] Gilliot, A., Morgand, S., Monnier, J.-C., Roy, J.-F. L., Geiler, C., and Pruvost, J., "Static and Dynamic SACCON PIV Tests, Part I: Forward Flowfield," *28th AIAA Applied Aerodynamics Conference*, American Institute of Aeronautics and Astronautics (AIAA), Chicago, Illinois, USA, 2010. https://doi.org/10.2514/6.2010-4395.

[15] Konrath, R., Roosenboom, E., Schröder, A., Pallek, D., and Otter, D., "Static and Dynamic SACCON PIV Tests, Part II: Aft Flow Field," *28th AIAA Applied Aerodynamics Conference*, American Institute of Aeronautics and Astronautics (AIAA), Chicago, Illinois, USA, 2010. https://doi.org/10.2514/6.2010-4396.

[16] Loeser, T., Vicroy, D., and Schuette, A., "SACCON Static Wind Tunnel Tests at DNW-NWB and 14'x22' NASA LaRC," *28th AIAA Applied Aerodynamics Conference*, American Institute of Aeronautics and Astronautics (AIAA), Chicago, Illinois, USA, 2010. https://doi.org/10.2514/6.2010-4393.

[17] Serpieri, J., "Cross-Flow Instability: Flow diagnostics and control of swept wing boundary layers," Ph.D. thesis, Delft University of Technology, 2018.

[18] Laar, Y., "Aerodynamic Design of a Flying V Aircraft in Transonic Conditions," Master's thesis, Delft University of Technology, Delft, The Netherlands, 2023.

[19] Laar, Y., Atherstone, D., Benad, J., and Vos, R., "Aerodynamic Design of a Flying V Aircraft in Transonic Conditions," *AIAA SCITECH 2024 Forum*, American Institute of Aeronautics and Astronautics (AIAA), Orlando, FL, 2024. https://doi.org/10.2514/6.2024-2669, 8-12 January 2024.

[20] Veldhuis, L., "Ijking Weegsysteem," Tech. Rep. LSW 88-12, Delft University of Technology, 1988.

[21] S. Bernardi, L. M., "Korte kalibratie van de balansen van de LTT windtunnel," Tech. rep., Delft University of Technology, 2008.

[22] Jorge, A. M. C. M., "Quantifying Wind Tunnel Effects on the Flying V," Master's thesis, Delft University of Technology, Delft, The Netherlands, 2023.

[23] Rediniotis, O., Hoang, N., and Telionis, D., "Multi-Sensor Investigation of Delta Wing High-Alpha Aerodynamics," *Proceedings of the 29th Aerospace Sciences Meeting*, American Institute of Aeronautics and Astronautics (AIAA), Reno, NV, USA, 1991. https://doi.org/10.2514/6.1991-735.

[24] Payne, F. M., Ng, T. T., and Nelson, R. C., "Seven hole probe measurement of leading edge vortex flows," *Experiments in Fluids*, Vol. 7, No. 1, 1989, pp. 1–8. https://doi.org/10.1007/BF00226590.

[25] Sforza, P. M., Stasi, W., Pazienza, J., and Smorto, M., "Flow Measurements in Leading-Edge Vortices," *AIAA Journal*, Vol. 16, No. 3, 1978, pp. 218–224. https://doi.org/10.2514/3.60880.

[26] Shaw-Ward, S., Titchmarsh, A., and Birch, D. M., "Calibration and Use of n-Hole Velocity Probes," *AIAA Journal*, Vol. 53, No. 2, 2014, pp. 336–346. https://doi.org/10.2514/1.J053130.

[27] Jeong, J., and Hussain, F., "On the identification of a vortex," *Journal of Fluid Mechanics*, Vol. 285, 1995, pp. 69–94. https://doi.org/10.1017/S0022112095000462.

[28] Zhou, J., Adrian, R. J., Balachandar, S., and Kendall, T. M., "Mechanisms for generating coherent packets of hairpin vortices in channel flow," *Journal of Fluid Mechanics*, Vol. 387, 1999, pp. 353–396. https://doi.org/10.1017/S002211209900467X.

[29] Mirande, J., Schmitt, V., and Werle, H., "Vortex Pattern Development on the Upper Surface of a Swept Wing at High Angle of Attack," , March 1979. URL https://ntrs.nasa.gov/citations/19790010743, presented at the AGARD Reunion on Aerodynamics of High Angles of Attack, Sandefjord, Norway, October 4-6, 1978.

[30] Poll, D. I. A., "Spiral Vortex Flow over a Swept-Back Wing," *Aeronautical Journal*, Vol. 90, No. 895, 1986, pp. 185–199. https://doi.org/10.1017/S0001924000015670.

[31] Pfnür, S., and Breitsamter, C., "Leading-Edge Vortex Interactions at a Generic Multiple Swept-Wing Aircraft Configuration," *Journal of Aircraft*, Vol. 56, No. 6, 2019, pp. 2093–2107. https://doi.org/10.2514/1.C035491.

[32] Ol, M., and Gharib, M., "Leading-Edge Vortex Structure of Nonslender Delta Wings at Low Reynolds Number," *AIAA Journal*, Vol. 41, 2003, pp. 16–26. https://doi.org/10.2514/2.1930.

[33] Lee, T., and Pereira, J., "Nature of Wakelike and Jetlike Axial Tip Vortex Flows," *Journal of Aircraft*, Vol. 47, No. 6, 2010, pp. 1946–1954. https://doi.org/10.2514/1.C000225.

[34] Gursul, I., Gordnier, R., and Visbal, M., "Unsteady aerodynamics of nonslender delta wings," *Progress in Aerospace Sciences*, Vol. 41, No. 7, 2005, pp. 515–557. https://doi.org/10.1016/j.paerosci.2005.09.002.

[35] Lynn, R., and Gursul, I., "Vortex Dynamics on a Generic UCAV Configuration," *44th AIAA Aerospace Sciences Meeting and Exhibit*, American Institute of Aeronautics and Astronautics (AIAA), Reno, Nevada, 2006. https://doi.org/10.2514/6.2006-61.

[36] Lucca-Negro, O., and O'Doherty, T., "Vortex breakdown: a review," *Progress in Energy and Combustion Science*, Vol. 27, No. 4, 2001, pp. 431–481. https://doi.org/10.1016/S0360-1285(00)00022-8.

[37] Luckring, J. M., and Hummel, D., "What was learned from the new VFE-2 experiments," *Aerospace Science and Technology*, Vol. 24, No. 1, 2013, pp. 77–88. https://doi.org/10.1016/j.ast.2011.07.012.

[38] Furman, A., and Breitsamter, C., "Turbulent and unsteady flow characteristics of delta wing vortex systems," *Aerospace Science and Technology*, Vol. 24, No. 1, 2013, pp. 32–44. https://doi.org/10.1016/j.ast.2012.08.007.

[39] Viviani, A., Aprovitola, A., Iuspa, L., and Pezzella, G., "Low Speed Longitudinal Aerodynamics of a Blended Wing-Body Re-Entry Vehicle," *Aerospace Science and Technology*, Vol. 107, 2020, p. 106303. https://doi.org/10.1016/j.ast.2020.106303.

[40] Smiley, T. D., Herman, C. C., Warner, R. M., Fagley, C. P., Ghoreyshi, M., and Seidel, J., "Experiments on Vortical Interactions on Generic Multi-Swept Wing Configurations," *AIAA AVIATION 2022 Forum*, American Institute of Aeronautics and Astronautics (AIAA), Chicago, IL & Virtual, 2022. https://doi.org/10.2514/6.2022-3303.

[41] Kwak, D., Hirai, K., Rinoie, K., and Kato, H., "Rolling Moment Characteristics at High Alpha on Several Planforms of Cranked Arrow Wing Configuration," *27th AIAA Applied Aerodynamics Conference*, American Institute of Aeronautics and Astronautics (AIAA), San Antonio, Texas, 2009. https://doi.org/10.2514/6.2009-3937.

[42] Konrath, R., Klein, C., and Schröder, A., "PSP and PIV investigations on the VFE-2 configuration in sub- and transonic flow," *Aerospace Science and Technology*, Vol. 24, No. 1, 2013, pp. 22–31. https://doi.org/10.1016/j.ast.2012.09.003.